Energy & Environmental Science

ROYAL SOCIETY OF CHEMISTRY

PAPER

View Article Online
View Journal | View Issue

Cite this: *Energy Environ. Sci.*, 2026, **19**, 1954

Battery aging assessment: from critical insights to enhanced diagnosis

Yunhong Che, *[ab] Joachim Schaeffer, [ac] Jinwook Rhyu, [a] Liang Wu,[a] Patrick A. Asinger,[a] Minsu Kim,[a] Jacob Sass,[a] Rolf Findeisen,[c] Martin Z. Bazant, [ad] William C. Chueh*[ef] and Richard D. Braatz *[a]

Received 28th October 2025,
Accepted 29th January 2026

DOI: 10.1039/d5ee06439b

rsc.li/ees

Reliable battery health diagnosis and cycle life prediction remain a central challenge for energy storage systems. This work first provides a systematic analysis of key factors for battery health diagnosis, highlighting previously overlooked yet critical elements that affect health assessments. Building on these insights, a rate-adaptive transformation model converts high C-rate features into low C-rate equivalents, enabling rapid diagnostics of battery aging modes without time-consuming testing using a low C-rate. To address fitting inaccuracies caused by aging, blended materials, and kinetic effects, an interpretable residual learning model corrects voltage mismatches, which also enables low C-rate fitting by using high C-rate data. Leveraging mechanistic-informed features, early cycle life prediction achieves mean errors of less than 70 cycles using data from fewer than 30 equivalent full cycles across complex and unseen aging conditions. This interpretable and generalizable framework bridges electrochemical understanding with practical diagnosis and offers a fast and reliable path toward mechanism-informed battery prognostics.

Broader context

Reliable and rapid battery health assessment is essential for ensuring safety, extending lifetime, and supporting large-scale electrification in transportation and renewable energy storage. Yet, accurate diagnostics often rely on slow laboratory tests and complex electrochemical modeling that are difficult to apply under real operating conditions. This work bridges the gap between mechanistic understanding and data-driven modeling to accelerate and improve battery health diagnosis. By systematically identifying key factors that influence diagnostic accuracy, the study introduces a rate-adaptive transformation to translate high-rate measurements into equivalent low-rate data and an interpretable residual learning model to correct degradation-induced voltage errors. Together, these methods allow fast, accurate, and explainable cycle life prediction using only limited early-cycle data. This framework not only enhances the reliability and interpretability of battery diagnostics but also provides a practical pathway toward efficient health management for large-scale battery systems, contributing to a more sustainable and circular energy future.

1 Introduction

Lithium-ion batteries have become the main energy storage technology in applications ranging from electric transportation and portable electronics to grid-scale storage and robotics systems.[1–3] As these systems grow in scale and complexity, ensuring their long-term reliability and safety is increasingly critical. In this context, accurate battery health diagnosis and cycle life prediction are essential for optimizing usage, preventing failures, and enabling predictive maintenance.[4–7] However, batteries degrade *via* complex, coupled electrochemical and mechanical processes, making it challenging to assess health states or predict end-of-life.

In practical applications, battery aging is typically characterized by cell-level indicators such as capacity and power fade. However, the underlying degradation stems from intricate electrochemical reactions that induce varying overpotentials due to transport limitations and reaction kinetics. These effects are further exacerbated under dynamic operating conditions,

[a] *Department of Chemical Engineering, Massachusetts Institute of Technology, Cambridge, MA 02139, USA. E-mail: yunhche@mit.edu, braatz@mit.edu*
[b] *Department of Energy, Aalborg University, Aalborg 9220, Denmark*
[c] *Control and Cyber-Physical Systems Laboratory, Technical University of Darmstadt, Darmstadt 64289, Germany*
[d] *Department of Mathematics, Massachusetts Institute of Technology, Cambridge, MA 02139, USA*
[e] *Department of Energy Science and Engineering, Stanford University, Stanford, CA 94305, USA. E-mail: wchueh@stanford.edu*
[f] *Applied Energy Division, SLAC National Accelerator Laboratory, Menlo Park, CA 94025, USA*

complicating both performance analysis and aging interpretation.[8–13] As a result, aging mode and electrode health diagnosis become increasingly important for in-depth aging evaluation, which can be achieved *via* physical modeling or data-driven approaches.[14–21]

Differential voltage fitting (DVF) has emerged as a widely adopted diagnostic tool for such purposes. By fitting the full-cell voltage profile to a reference half-cell model, DVF effectively scales and shifts the open-circuit potentials (OCPs) of the anode and cathode, enabling the quantification of key degradation modes such as loss of lithium inventory (LLI) and loss of active material (LAM).[13,22–27] To minimize kinetic distortion and accurately capture equilibrium behavior, DVF is ideally performed at extremely low current rates (*e.g.*, C/40). However, such conditions are relatively hard for routine diagnostics due to their excessive time requirements, downtime requirements during operations, and may perturb aging trajectories. Higher C-rate measurements offer improved efficiency but introduce kinetic artifacts that degrade diagnostic accuracy. Recent advances have sought to overcome this challenge using machine learning models to infer low C-rate behavior from high C-rate data.[28–30] Nevertheless, these data-driven approaches often lack physical interpretability and struggle to generalize across different battery chemistries and aging scenarios, thereby limiting their robustness and scalability. Physics-constrained models can improve interpretability, but it is still hard to identify key intrinsic relations between different C-rate measurements.[31,32]

The accuracy of DVF can deteriorate over time due to reference OCP shifts, voltage hysteresis, and the evolving nature of aging mechanisms. These factors introduce systematic fitting errors that compromise the reliability of electrode-level health indicators. To address this, previous studies have introduced additional fitting parameters, such as the silicon ratio in blended anodes, to adjust the anode's reference OCP and improve fitting accuracy.[33–37] However, battery aging is a coupled, multi-physics process, especially in hybrid electrodes with multiple active materials, and changes in the cathode OCP can also play a significant role. These observations highlight that DVF fitting errors during aging are not isolated artifacts, but manifestations of complex, interacting degradation pathways. Therefore, compensating for these effects requires a more holistic and adaptive modeling framework that can evolve with the battery's aging.

Beyond current health diagnostics, predicting battery cycle life remains a critical yet challenging task, particularly under complex aging conditions. Cycle life prediction has become a critical enabler in battery research, accelerating material discovery, guiding cell design, facilitating predictive maintenance, and informing second-life deployment strategies.[21,38–40] Early prediction is even more difficult, as batteries typically exhibit minimal degradation during the initial cycles. Nevertheless, early cycle life prediction offers significant benefits, including accelerated battery R&D at lower cost and improved maintenance strategies, making it a topic of global research interest. While recent advances in data-driven approaches have demonstrated strong predictive performance, many models depend on features that are highly sensitive to specific usage conditions, which limits their ability to generalize across diverse aging scenarios.[41–44] In parallel, deep learning techniques offer enhanced accuracy but often do so at the cost of interpretability, hindering trust and obscuring physical insights.[45–47] To address these challenges, models grounded in physically meaningful features and interpretable structures provide a compelling pathway toward accurate, robust, and generalizable cycle life prediction.[24,38,48,49]

In this work, we first conduct a systematic evaluation of DVF performance using OCV measurements at different C-rates, revealing critical limitations and offering actionable insights for more reliable and robust health diagnostics. Guided by these findings, we develop a simple yet interpretable transformation model that accurately predicts low C-rate electrode behavior from high C-rate measurements, enabling faster and more reliable mechanism interpretation. To further address residual fitting errors, particularly those exacerbated by aging, we introduce an interpretable residual learning model that corrects degradation-induced deviations. This hybrid framework combines mechanistic understanding with data-driven learning, enabling robust extraction of electrode health under diverse aging conditions. Notably, the residual model also allows reconstruction of low C-rate OCV curves with high C-rate measurements, substantially reducing diagnostic time while ensuring reliable health mechanism diagnosis in practical settings. Finally, leveraging the extracted mechanistic features, we demonstrate accurate early cycle life prediction using only the first 30 equivalent full cycles (EFCs), achieving a mean absolute error of fewer than 69 EFCs across a wide range of previously unseen protocols. Overall, this study advances hybrid DVF modeling with C-rate adaptability and establishes a unified, interpretable framework for accurate and explainable battery health diagnosis and cycle life prediction.

2 Results

2.1 Data description

To evaluate the DVF effectiveness and the proposed residual compensation comprehensively, data with different C-rates are considered in this work. Specifically, three datasets are used, which are the reference performance tests (RPT) dataset with both C/5 and C/40 tests generated by Che *et al.*[31] (named Dataset 1), the cycling dataset with a periodic C/5 RPT test generated by van Vlijmen *et al.*[24] (named Dataset 2), and the cycling dataset with a periodic C/40 RPT test generated by Geslin *et al.*[13] (named Dataset 3). More descriptions of the three tests can be found in the Experiment section and are detailed in the respective reference papers,[13,24,31] and we specify the purpose of using each of the three datasets below.

Firstly, we use Dataset 1 for DVF fitting with discussions of key remarks and issues influencing fitting performance, and demonstrate the correlation between the electrode features extracted from C/5 and C/40, showing the possibility and

reasonability of transforming low C-rate RPTs to high C-rate RPTs in battery health diagnosis. Then, we discuss the challenge of DVF to track the aging mechanisms accurately in different aging conditions and how the effectiveness of DVF deteriorates during aging for both C/5 and C/40 OCV fitting, quantifying the reliability of DVF during aging and the dependency on C-rates. Building on these results, we use all three datasets for the evaluation of the proposed learning-based residual compensation. Finally, Dataset 2, which involves various aging patterns and loading protocols, is used for the interpretable and early cycle life predictions with respect to unseen aging conditions.

2.2 Health diagnosis

2.2.1 Remarks and key issues. In DVF, key mechanistic parameters are extracted by scaling and shifting reference half-cell OCP curves to match full-cell OCV measurements, as described in Methods. The optimization process is critical for reliable parameter identification and must be carefully designed to ensure trustworthy results. Various optimization algorithms, such as particle swarm optimization (PSO), differential evolution (DE), Bayesian optimization (BO), genetic algorithms (GA), and covariance matrix adaptation evolution strategy (CMA-ES), can be employed for this purpose. Due to the non-uniqueness of the solution space, multiple fitting runs are required to assess robustness. To evaluate both accuracy and robustness, we perform 10 independent fittings starting with different initials for each cell in the first dataset using different optimization algorithms, with the resulting errors in Fig. 1A–C and Fig. S1–S3. The fitting performance varies significantly across algorithms and trials, with DE and CMA-ES having more consistent convergence, which indicates the high robustness of obtaining more reliable fitting results and mechanism parameters. In contrast, GA produced the least accurate fits with the

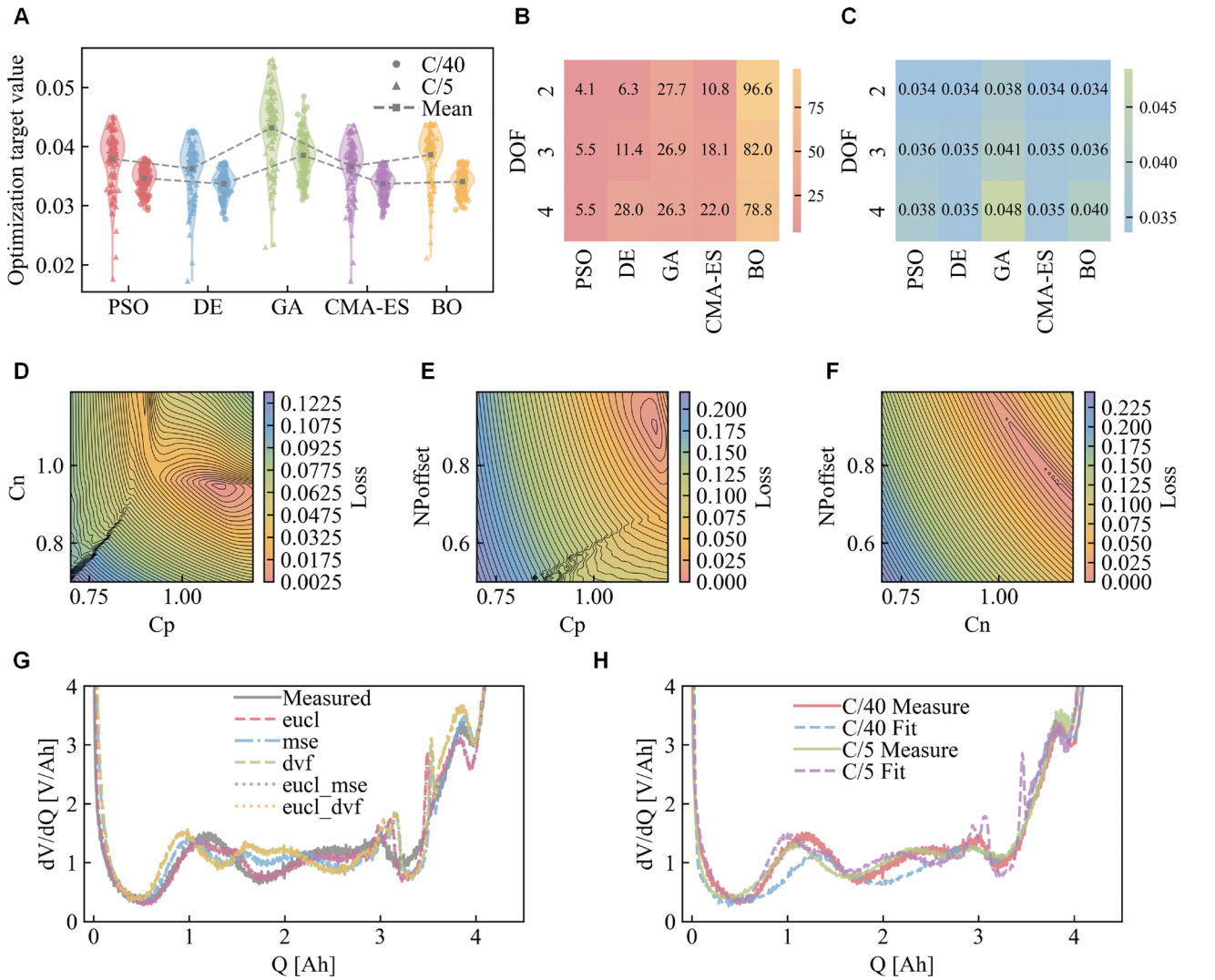

Fig. 1 Fitting evaluation with different settings. (A) Distributions of the best fitting results of the 94 cells in 10 rounds with different optimization algorithms. (B) Time consumption for different optimization algorithms and DOFs. (C) Values of the Euclidean objective functions with different optimization algorithms and DOFs. (D)–(F) Identifiability analysis of the model parameters. (G) Example differential voltage curve with different objective functions using DE with 3 DOF. (H) Example DV curve with mismatched C-rates between the full cell and half cells.

lowest robustness, while BO is time-consuming. Importantly, even when the overall fitting errors are similar, the underlying parameter sets may diverge significantly, resulting in discrepancies in the evaluation of electrode degradation. Therefore, robust and reproducible fitting is essential to ensure reliable parameter identification for the interpretation of battery degradation mechanisms.

Different degrees of freedom (DOF) can be defined in DVF-based battery health diagnosis depending on assumptions regarding half-cell OCP variations. Here, we compare fitting results under 2-, 3-, and 4-DOF settings and discuss the implications of each approach (see Methods for implementation details).[22,24,50] Under the 2-DOF configuration, only the capacity ratio between the cathode and anode and their relative offset are considered. While this yields good fits to full-cell OCV curves and enables fast computation, it lacks the ability to decouple electrode-specific degradation. As a result, the method implicitly assumes that aging occurs in only one electrode, limiting its diagnostic interpretability. The 3-DOF model introduces an additional degree of freedom by allowing one electrode (*e.g.*, the anode) to scale independently. This method enables the identification of degradation in a specific electrode while maintaining computational efficiency. Compared to the full 4-DOF model, which accounts for independent shifts in both electrodes, the 3-DOF setting achieves similar fitting performance of accuracy for the tested cells (Fig. 1C) with high robustness, as the cathode exhibits minimal shift across cycling. Given the full-rank observability of mechanistic parameters confirmed *via* Jacobian analysis (Fig. S4), and the lower computational cost in Fig. 1B, we adopt the 3-DOF model throughout this work. However, this choice may need to be revisited for other cell chemistries where more significant shifts in both electrodes occur. In addition, the loss variations with respect to pairwise parameter perturbations are in Fig. 1D–F, while the loss evolution over iterations is in Fig. S4. These results collectively reflect the identifiability of the estimated parameters. The results reveal strong interdependence among the three parameters, with the offset parameter being particularly challenging to identify. The iterative process also reveals the presence of multiple local minima during parameter estimation, further highlighting the importance of conducting multiple rounds of optimization to ensure robust mechanistic parameter estimations.

The third critical factor in DVF performance lies in the definition of the objective function. The most direct approach evaluates the difference between the fitted and measured OCV curves, typically using the mean squared error (mse) of the voltage values, as the measured capacity is fixed and used as input. However, DVF models also aim to preserve the fidelity of the differential voltage curve, which captures key degradation signatures. To this end, we consider another loss function based on the difference in differential voltage (dvf), which promotes accurate aging mode identification and increases the sensitivity/weight to voltage changes due to phase transformations. Beyond direct voltage- or derivative-based losses, we introduce a Euclidean distance loss (eucl) that constrains the overall curve shape, providing a global regularization to maintain physical consistency. As shown in Fig. 1G, different objective functions yield distinct fitting results for the same cell. The Euclidean loss, in particular, preserves curve morphology more faithfully and shows higher stability across conditions (see also Fig. S1–S3). The detailed formulations are described in Methods.

Besides the three key factors discussed above, the selection of reference half-cell OCP curves for scaling and shifting is also crucial, as the shape of the half-cell OCP directly determines the underlying form of the full-cell OCV curve. Ideally, the C-rate used for testing the half-cell OCP should match that of the full-cell OCV. This alignment ensures that the scaled and shifted half-cell OCP curves accurately represent the full-cell OCV shape under the same C-rate condition. To illustrate the impact of mismatched C-rates, we present fitting results in Fig. 1H using inconsistent half-cell OCPs for full-cell OCV reconstruction—specifically, applying C/5 OCP curves to fit C/40 OCV data, and *vice versa*. The results show clear deviations between the fitted and measured curves in both scenarios. When low C-rate (C/40) half-cell OCPs are used to fit high C-rate (C/5) full-cell OCVs, the resulting curves display additional features not observed in the measurements. Conversely, using high C-rate OCPs to fit low C-rate OCVs fails to capture some mechanistic features present in the measurements. The implications of these mechanistic distortions will be further explored in the next subsection.

There are some other key issues that limit the fitting effectiveness in DVF. One major assumption is that the full-cell OCV can be reconstructed solely by scaling and shifting the pristine electrode OCP curves. However, this neglects electrode aging, which can significantly alter electrode kinetics, capacity ratios, and active material utilization. Moreover, half cells have to be physically harvested and constructed from full cells, introducing potential experimental artifacts. Such changes distort the shapes of the reference half-cell OCP curves, particularly for hybrid electrodes with multiple, multiphase active materials, such as silicon–graphite anodes,[51] and are also observed in various cathode chemistries. Materials such as lithium iron phosphate (LFP) exhibit strong voltage hysteresis between charge and discharge, related to reaction-controlled phase separation,[52–55] complicating consistent curve fitting across cycles in diagnostic tests. Additionally, temperature variations, kinetic overpotentials, and C-rate-dependent effects related to these nonlinear phenomena introduce further discrepancies between the fitted and actual differential voltage curves. Measurement noise and the non-uniqueness of the solution space also make it challenging to identify the underlying aging mechanisms reliably. In practice, filtering techniques are often applied to the raw differential voltage curves to reduce noise and extract key features such as peak and valley positions and magnitudes. However, excessive smoothing may compromise the fidelity of aging-relevant features, requiring a careful balance between denoising and feature preservation. Moreover, cell-to-cell variability and mechanical degradation, such as electrode cracking or separator deformation, can also introduce

subtle but impactful differences in the DVF behavior, especially over long-term cycling. These effects are difficult to capture with purely physics-based models. To address these limitations, we propose a machine learning-based compensation approach for the unknown or unmodeled mechanisms in DVF, which is discussed in detail later in this article.

2.2.2 Mode analysis and predictions. The fitted states of the mechanistic model represent electrode degradations (LAM, represented by the electrode capacity loss) and LLI (captured by the depletion of cyclable lithium (Q_{li})). These degradation metrics can be inferred non-destructively (see Methods for detailed derivations). Given that DVF profiles vary significantly with C-rate, it is crucial to assess the consistency of degradation features extracted under different testing conditions. As shown in Fig. S5, parity plots of positive (C_p) and negative (C_n) electrode capacities, as well as lithium inventory (Q_{li}), exhibit strong linear correlations between C/5 and C/40 tests, with high goodness-of-fit from linear regressions. These findings demonstrate the good robustness of DVF-based health indicators identification across C-rates and validate the use of higher C-rate diagnostics for practical battery health assessments. In addition, the consistency of the degradation on both electrodes and the active lithium demonstrates that both LAM and LLI happen during the constant current cycling with different C-rates applied.

To enable fast and interpretable electrode state estimation and understanding of the degradation mechanism, we employ a sparse multi-task model that maps high C-rate OCV-derived features to their low C-rate counterparts. Unlike traditional approaches that rely on multiple independent regressors (*e.g.*, Lasso and Elastic Net), we adopt a unified multi-task Lasso to simultaneously predict multiple mechanistic states, including full-cell capacity (C_q) and electrode-specific descriptors (C_p, C_n, Q_{li}). The model is trained and validated on 94 cells using 50 randomized train-validation-test splits (60%–20%–20%), with hyperparameters optimized *via* cross-validation. Representative results for moderate prediction accuracy are in Fig. 2A–F, with best and worst cases detailed in Fig. S6 and S7. The model accurately recovers low C-rate states from C/5 features, achieving mean absolute errors (MAE) and root mean squared errors (RMSE) below 2.85% and 2.52%, respectively (Fig. 2C and Table S1). In addition to its predictive performance, the model is inherently interpretable: the learned feature weights reveal the relative importance of each input, offering insight into dominant degradation pathways. Capacity from the high C-rate has the overall highest impact; electrode capacity and lithium inventory show significant impact, indicating the importance of considering both LAM on cathode and anode, as well as LLI for the health diagnosis. This sparse structure facilitates efficient aging mode identification under high C-rate protocols, enabling the fast diagnosis of both LAM and LLI for interpretation of degradation patterns.

Despite the mismatched OCP curves, as discussed in the above section, the mechanistic states obtained from DVF remain highly consistent with those derived from matched fittings. As shown in Fig. 2G–I, the positive electrode capacity (C_p) extracted from the C/40 full-cell OCV curve using the C/5 half-cell OCP profiles exhibits a strong linear correlation ($R > 0.9$) with the value obtained using the matched C/40 OCP curves. This high degree of linearity is preserved across all three aging modes, demonstrating that mismatched OCP inputs can still yield reliable mechanistic interpretations. These results suggest that a simple linear transformation suffices to bridge the discrepancy introduced by OCP mismatches. Therefore, DVF can be flexibly implemented in practical scenarios, including under higher C-rate conditions or when only unmatched OCP data are available.

2.2.3 Aging pattern reconstruction. Building on the findings above, we reconstructed more realistic electrode degradation trajectories by mapping high C-rate (C/5) test results to low C-rate (C/40) aging modes. The inferred electrode health states under C/5 and the predicted C/40 counterparts, derived *via* the interpretable model, are in Fig. 3A, with two representative cells exhibiting super-linear and sub-linear aging behaviors. Specifically, the super-linear aging cell exhibits accelerated loss of both positive and negative electrode capacities after the ''knee'' point, suggesting the onset of coupled degradation mechanisms such as lithium inventory loss amplified by structural or interfacial instability. In contrast, the sub-linear aging cell shows a more gradual and decelerating degradation trend, consistent with early-stage interfacial growth processes (*e.g.*, SEI thickening) that progressively self-limit reaction kinetics and active material utilization.[56] Notably, the aging mode values extracted from C/5 data are consistently lower than those projected for C/40, indicating the healthier status of the electrodes and electrolyte compared to the observed conditions. This discrepancy arises from kinetic and resistive effects inherent to high C-rate operation, which obscure the true thermodynamic degradation.[54,55,57–59] By applying an interpretable transformation model, we enable the reconstruction of aging patterns that more accurately reflect intrinsic cell health.

Using this model, we can reconstruct more realistic degradation patterns that would otherwise require low C-rate (C/40) diagnostic tests to reveal. Fig. 3B presents the reconstructed aging trajectories for all cells in Dataset 2, tracking the capacity loss of the cathode and anode (reflecting LAM for each electrode), the loss of active lithium ions (LLI), and the resulting full-cell capacity fade under diverse and complex aging patterns. Different cycling conditions result in different aging patterns containing different contributions from LAM and LLI, which are interpretable through our model. Additional representative cells with varying cycle lives and degradation patterns, along with their original C/5-based fitting results, are in Fig. S8. Generally, the C/5 fitting results give an overestimation of the aging conditions, *i.e.*, LLI and LAM, while the cathode degradation (representing LAM_p) may be underestimated in early aging stages. This discrepancy is further illustrated in Fig. 3C and D, where the reconstructed OCV and differential voltage (dV/dQ) curves under C/40 conditions are compared to C/5-based results for a representative cell exhibiting super-linear aging. The observed differences highlight how kinetic limitations and internal resistances at higher C-rates

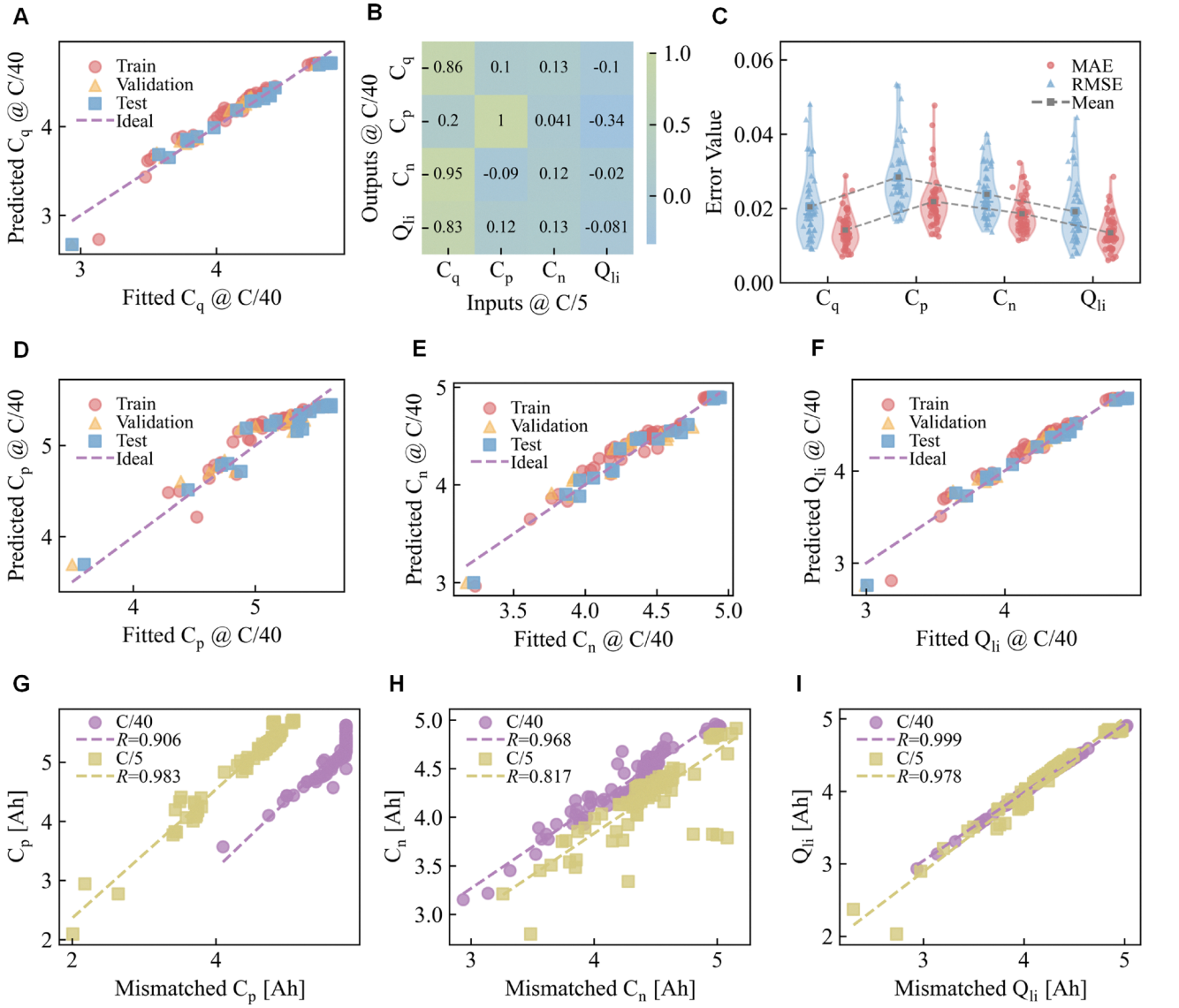

Fig. 2 Electrode health predictions. The models take the measured capacity and the fitted parameters from C/5 for the predictions of the corresponding conditions under C/40. (A) Predictions for the C_q. (B) Model interpretations of the feature contributions. (C) Error distributions for the predictions of all cells. (D) Predictions for the C_p. (E) Predictions for the C_n. (F) Predictions for the Q_{li}. (G)–(I) Relationships of the C_p, C_n, Q_{li} between C/40 and C/5 with mismatched C-rates between the half-cell OCPs and the full-cell OCV.

can obscure the true thermodynamic degradation, leading to a misjudgment of battery health. Through the variations of the key features, like the peaks and valleys of the reconstructed differential voltage curves, battery aging mechanisms can be interpreted. Notably, the widening gaps between the RPT cycle in the OCV and differential voltage curves accurately reflect the accelerated aging after the knee onsite. Nevertheless, the predictor still shows effective boundaries on the mechanism reconstruction, especially for mechanisms influenced by the blended electrodes and aging, which distorted the shapes of the OCV curves. In addition, the predictor still shows some mismatches in some cases. In such cases, even small fitting mismatches may lead to disproportionately large deviations in the inferred aging modes (*e.g.*, LLI/LAM decomposition) and peak-related mechanistic interpretation. These limitations motivate the residual compensation introduced in the following section to correct systematic deviations and improve the fidelity of mechanism reconstruction.

2.3 Learning residuals through machine learning

2.3.1 Machine learning compensation for DVF model. Despite its widespread use, the mechanistic model struggles to fully capture electrode aging mechanisms due to kinetic limitations and aging-induced inconsistencies. As shown in Fig. 1G and H, residuals persist between the measured and fitted OCVs, even after extensive optimization. As demonstrated in Fig. 4A, fitted errors (representing the differences between the fitted curves and the real curves) enlarge over aging, which diminishes key aging features. The errors are even larger in some state of charge (SOC) ranges, especially for deep discharge

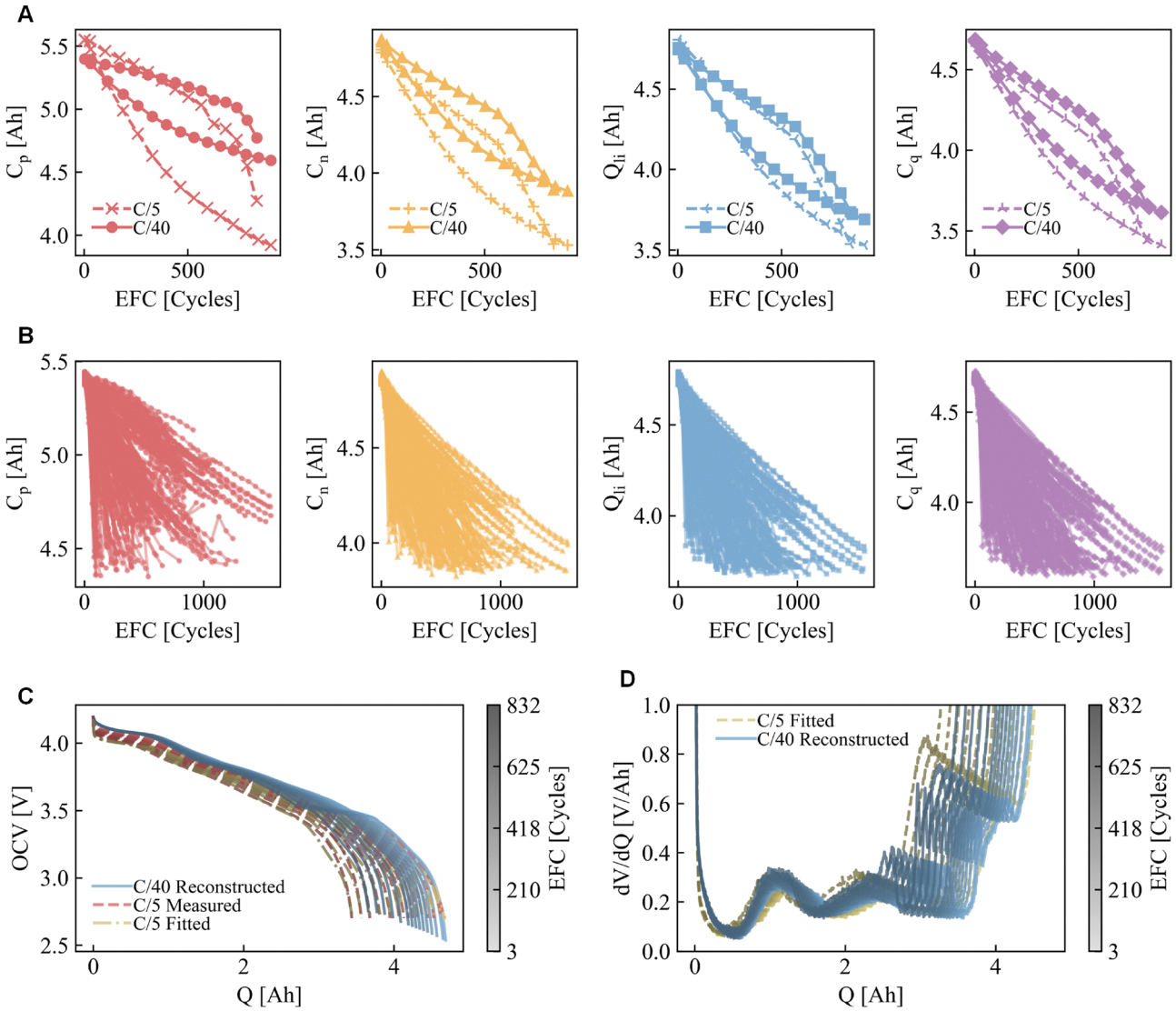

Fig. 3 Aging pattern reconstruction. (A) Reconstruction of the aging patterns under C/40 using measurements from C/5 for two cells that have sub-linear and super-linear degradation trajectories. (B) Reconstruction of the aging patterns under C/40 using measurements from C/5 for all cells in Dataset 2. (C) Reconstruction of the OCV curves of one representative cell under C/40 using measurements from C/5. (D) Reconstruction of the differential voltage curves of one representative cell under C/40 using measurements from C/5.

(low SOC) regions, where transport and interfacial resistances increasingly limit electrochemical accessibility. In cells employing silicon–carbon blended anodes, large volume changes, interfacial instability, and repeated SEI reformation exacerbate impedance growth, effectively preventing the full utilization of remaining lithium inventory before the voltage cutoff is reached. As a result, conventional DVF-based fitting overestimates apparent capacity loss and fails to faithfully represent intrinsic electrode degradation. These discrepancies are more pronounced under high C-rate (C/5) conditions than at lower C-rates (C/40), suggesting that conventional DVF can severely misrepresent degradation under realistic operating scenarios.

We introduce a machine learning-based residual compensation strategy that enhances the fitting accuracy of mechanistic models by correcting their systematic errors. This machine learning residual makes the compensation originate from different sources during aging and is informed by mechanistic states as model input. Although the half-cell DVF model alone exhibits limited fitting accuracy, the mechanistic features that it extracts remain stable across different aging and C-rate conditions. These physically meaningful features representing the electrode health condition and the amount of active lithium, derived from either low or high C-rate data, provide a robust foundation for the learning model, thereby improving both its interpretability and extrapolation capability. As illustrated in Fig. 4C, the extracted mechanistic features Φ, which are obtained from the classical DVF framework, are fed into a residual learner, which predicts the pointwise residuals of the fitted OCV curve. These predicted residuals are then added to the baseline DVF model to yield an enhanced overall fit. Details

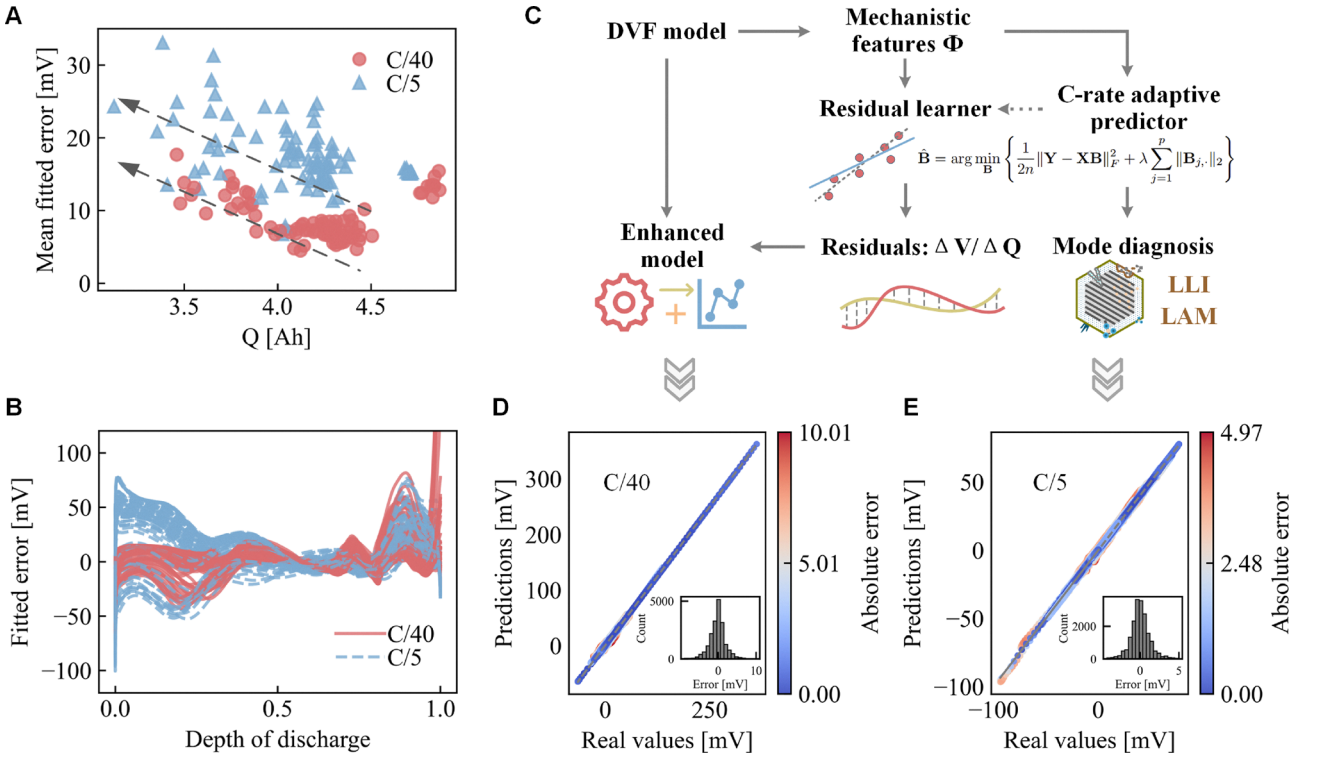

Fig. 4 Residual compensations using machine learning. (A) Demonstration of the mean DOF errors of the cells with different SOHs and C-rates. (B) Errors of the fitted OCV errors with respect to different DODs. (C) Flowchart for the machine learning based residual compensations. (D)–(E) Compensation results for the C/40 and C/5 curves respectively.

of the model structure are provided in Methods. When applying the model across different C-rates, the rate-adaptive predictor introduced earlier is used to estimate the mechanistic features at the target C-rate. These predicted features are subsequently passed to the residual learner for residual compensation. Both the predictor and the residual learner adopt sparse and interpretable formulations, based on Lasso and multi-task Lasso. Using Dataset 1 with random data split with ratios of 6:2:2 for the training, validation 1, and validation 2 (testing) for both C/40 and C/5 OCV curves, the model achieves high accuracy and generalizability. As shown in Fig. 4D, E and Table 1, the MAE is reduced from over 17 mV to below 1.5 mV. Notably, the maximum absolute error decreases dramatically from 361.6 mV to under 10.1 mV substantially mitigating previously observed high-error regions (Fig. 4B).

We further applied the residual compensation model to enhance health diagnostics during battery aging, enabling aging mechanisms interpretation during applications. Trained on cells with varying SOHs from Dataset 1 and tested on Dataset 2, the model substantially improves the fit of differential voltage curves, as shown in Fig. S9. To validate the generalization capability, we retrained the model on a subset of cells and evaluated it on cells exhibiting unseen aging conditions.[31] The resulting performance, illustrated in Fig. 5A, shows prediction errors consistently below 21.7 mV, with most errors tightly clustered around zero. Beyond improved fitting accuracy, the proposed hybrid model preserves and reconstructs key physical features that are critical for aging assessment, including indicators associated with LLI and LAM. As shown in Fig. 5B

Table 1 Summary of the residual compensation for different datasets and C-rates

Objective	Method	RMSE	MAE	MaxAE	R^2
Dataset 1 C/5	Residual compensation	1.21 mV	0.89 mV	4.97 mV	1.000
	Original fitting	22.94 mV	17.10 mV	93.61 mV	0.997
Dataset 1 C/40	Residual compensation	2.06 mV	1.48 mV	10.01 mV	1.000
	Original fitting	18.72 mV	8.40 mV	361.65 mV	0.997
Dataset 2 C/5	Residual compensation	3.64 mV	2.45 mV	30.61 mV	1.000
	Original fitting	26.76 mV	18.64 mV	131.86 mV	0.996
	Compensation (retrain)	1.37 mV	0.95 mV	21.70 mV	1.000
Dataset 3 C/40	Residual compensation	3.01 mV	2.01 mV	131.35 mV	1.000
	Original fitting	30.58 mV	18.27 mV	240.99 mV	0.992
	Compensation	1.87 mV	0.96 mV	99.94 mV	1.000
Dataset 1C/5 to C/40	Voltage compensation	4.56 mV	3.32 mV	17.53 mV	0.991
	Capacity compensation	21.55 mAh	16.49 mAh	67.23 mAh	0.877

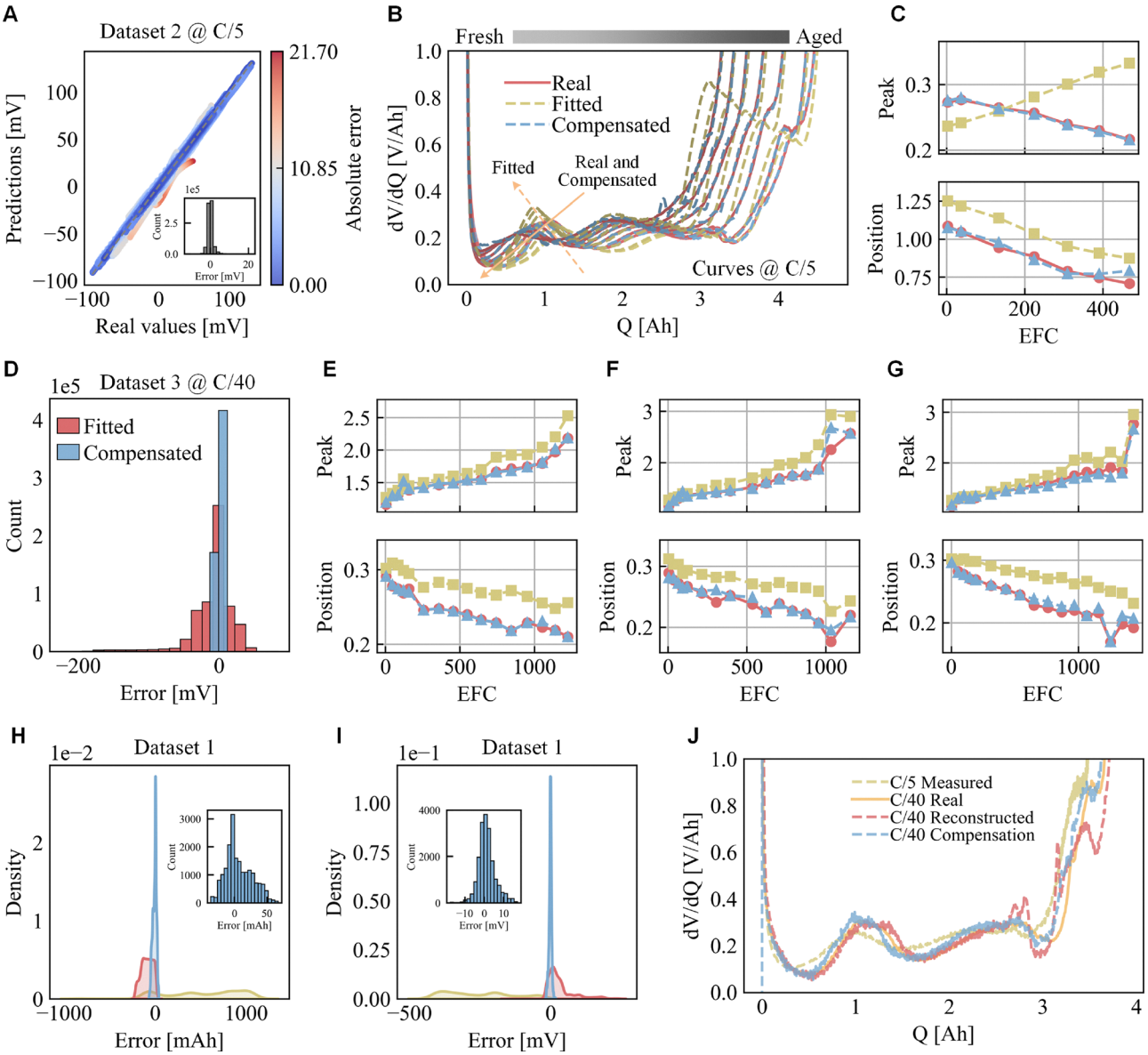

Fig. 5 Residual compensations for enhanced aging reconstruction. (A) The compensation results for the testing cells in Dataset 2 and the error distributions. (B) Differential voltage curves of one representative cell during aging and the demonstration of the inefficient fittings and the enhanced fittings by machine learning. (C) Aging reconstruction capability of the original model and the enhanced model. (D) The compensation results for the testing cells in Dataset 3 and the error distributions. (E)–(G) Aging reconstruction capability of the original model and the enhanced model for three representative cells aged with highway, urban, and real city loadings, respectively. (H) and (I). Residual compensations from C/5 to C/40 for the capacity and voltage residuals, respectively. (J) Demonstration of one cell for the residual compensation from C/5 to C/40.

for a representative cell tracked across its full aging trajectory, conventional DVF increasingly fails to reproduce aging-induced changes in the voltage profile, particularly in deep depth-of-discharge (DOD) regions. This limitation arises from the underlying assumption of DVF that degradation effects can be fully represented by scaling and shifting of reference OCP curves, which becomes invalid as aging introduces heterogeneous kinetics, transport limitations, and interfacial resistance growth.

By contrast, the proposed hybrid framework explicitly compensates DVF residuals while retaining its physically interpretable backbone, enabling the recovery of both the global evolution of the differential voltage response and localized aging signatures. In particular, the model successfully reconstructs the gradual disappearance of low-SOC shoulder and inflection features with cycling. These features are commonly associated with phase-transition-related processes and stoichiometric plateaus, whose voltage signatures become progressively obscured as degradation advances. From a mechanistic perspective, such suppression is consistent with degradation pathways widely reported in blended anodes, where repeated lithiation-induced volume expansion of silicon phases leads to particle cracking, electrical isolation, and the formation of

electrochemically inactive domains. This process couples LAM with LLI through the trapping of lithium in isolated regions and interfacial layers, thereby reducing electrochemical accessibility prior to the voltage cutoff. Concurrently, accumulated interfacial degradation amplifies polarization effects, causing the voltage response in deep DOD regions to become increasingly dominated by kinetic limitations. Importantly, the hybrid model captures the systematic shift of peak positions and the monotonic attenuation of peak magnitudes with cycling, as summarized in Fig. 5C. These coordinated trends reflect the coupled evolution of lithium redistribution and active material degradation, providing physically interpretable markers of aging progression rather than fitting artifacts. Together, these results demonstrate that the hybrid framework enables mechanistic insight into battery aging pathways under realistic operating conditions, beyond what is accessible with conventional DVF analysis alone. As summarized in Table 1, the improved model achieves the MAE of less than 2.45 mV across all testing cells in Dataset 2.

We then applied our model to Dataset 3, which includes a different commercial battery type and provides OCV curves during dynamic aging measured at C/40. The original fitted electrode states are plotted in Fig. S10. The error distributions before and after using the residual compensation are plotted in Fig. 5D, and the numerical results are listed in Table 1, where the errors are significantly reduced by introducing the proposed residual model. The model's ability to reconstruct aging patterns is demonstrated in Fig. 5E–G for three representative cells subjected to highway, urban, and real city driving profiles with differential voltage curves reconstruction in Fig. S10. In each case, the magnitude of the first voltage peak and the corresponding capacity are highlighted as the two key features characterizing the differential voltage curve. While the fitted curves capture the general trend of the peak shift during aging, they still deviate notably from the ground truth, typically overestimating the peak magnitude. The residual model effectively corrects these discrepancies, thereby enhancing the accuracy (with MAE of less than 0.97 mV) of battery aging diagnosis. Note that the filtering is needed in Dataset 3 since the original curves are noisy for feature extraction, as demonstrated in Fig. S10.

2.3.2 Taking compensation for high C-rates. Although low C-rate RPTs are preferable for accurate aging diagnosis, they are time-consuming and impractical for real-world applications. As discussed earlier, the rate-adaptive predictor effectively transforms mechanistic states from high to low C-rate with high accuracy. Therefore, we extend the residual compensation model to account for the discrepancies between the fitted OCV curve derived from high C-rate tests and the target low C-rate OCV curve, enabling more accurate health diagnostics with reduced testing time. In this case, both voltage and capacity residuals must be compensated, as the latter also affects the reconstruction of low C-rate OCV curves. The rate-adaptive prediction provides estimates of full-cell and electrode capacities, which are then interpolated at constant intervals for OCV reconstruction. However, residuals still exist in both voltage and capacity domains, as illustrated in Fig. S11. Hence, our approach includes two components: voltage and capacity residual compensations. The results are in Fig. 5H–J, where the overall results and the specific result for one cell are presented. The reconstruction accuracy improves progressively in the order of C/5 direct measurement, C/40 mechanistic reconstruction, and C/40 residual compensation. As summarized in Table 1, the MAE for the capacity and voltage compensation is less than 16.50 mAh and 3.32 mV, respectively.

The reconstruction of aging degradation from high C-rate measurements to low C-rate expectations can be further improved by incorporating the residual learning model. Fig. S12 illustrates the variation across the original C/5 curves, the reconstructed C/40 curves from the rate-adaptive predictor, and the final enhanced curves with residual correction for a representative cell. While the rate-adaptive model captures the dominant rate-dependent trends, the residual correction further refines the curve morphology, particularly in low-SOC regions where voltage responses are strongly influenced by aging-induced polarization and resistance growth. Overall, by integrating the DVF framework with rate-adaptive prediction and machine learning-based residual compensation, we achieve more accurate and efficient battery health diagnostics. This approach enables deeper insights into battery degradation under complex aging scenarios, while significantly reducing testing time and resource consumption.

The above results demonstrate that the proposed hybrid and interpretable framework enables enhanced battery health diagnosis under complex cycling conditions, with improved modeling of residuals arising from aging-related kinetics, polarization, and degradation-induced parameter evolution. Other battery chemistries may exhibit distinct electrochemical characteristics that introduce additional challenges. For example, LFP cells show flat open-circuit voltage profiles and pronounced hysteresis behavior, which can affect observability and residual structures and are not explicitly addressed here. Nevertheless, the proposed framework is not restricted to any specific battery chemistry, as it systematically combines explicit mechanistic models with data-driven compensation and can be extended to alternative chemistries by incorporating appropriate mechanistic representations and targeted data.

2.4 Cycle life prediction

Here, we demonstrate interpretable cycle life prediction for batteries aged under diverse protocols, using data from an early stage ($\sim$30 EFC, less than 10% of the lifespan), where visible degradation is minimal. Fig. 6 presents the prediction results: panel A shows feature contributions from the model, panel B illustrates a parity plot of predicted and actual cycle life, and panel C highlights interpretable results on feature contributions calculated from the Lasso model across different SOH thresholds. Corresponding numerical results are summarized in Table 2. The model is evaluated on two validation sets: validation set 1 comprises a 20% subset of the initial training data, while validation set 2 (original testing data for unseen cells) includes cells aged under previously unseen protocols, providing a rigorous evaluation of extrapolation capability and

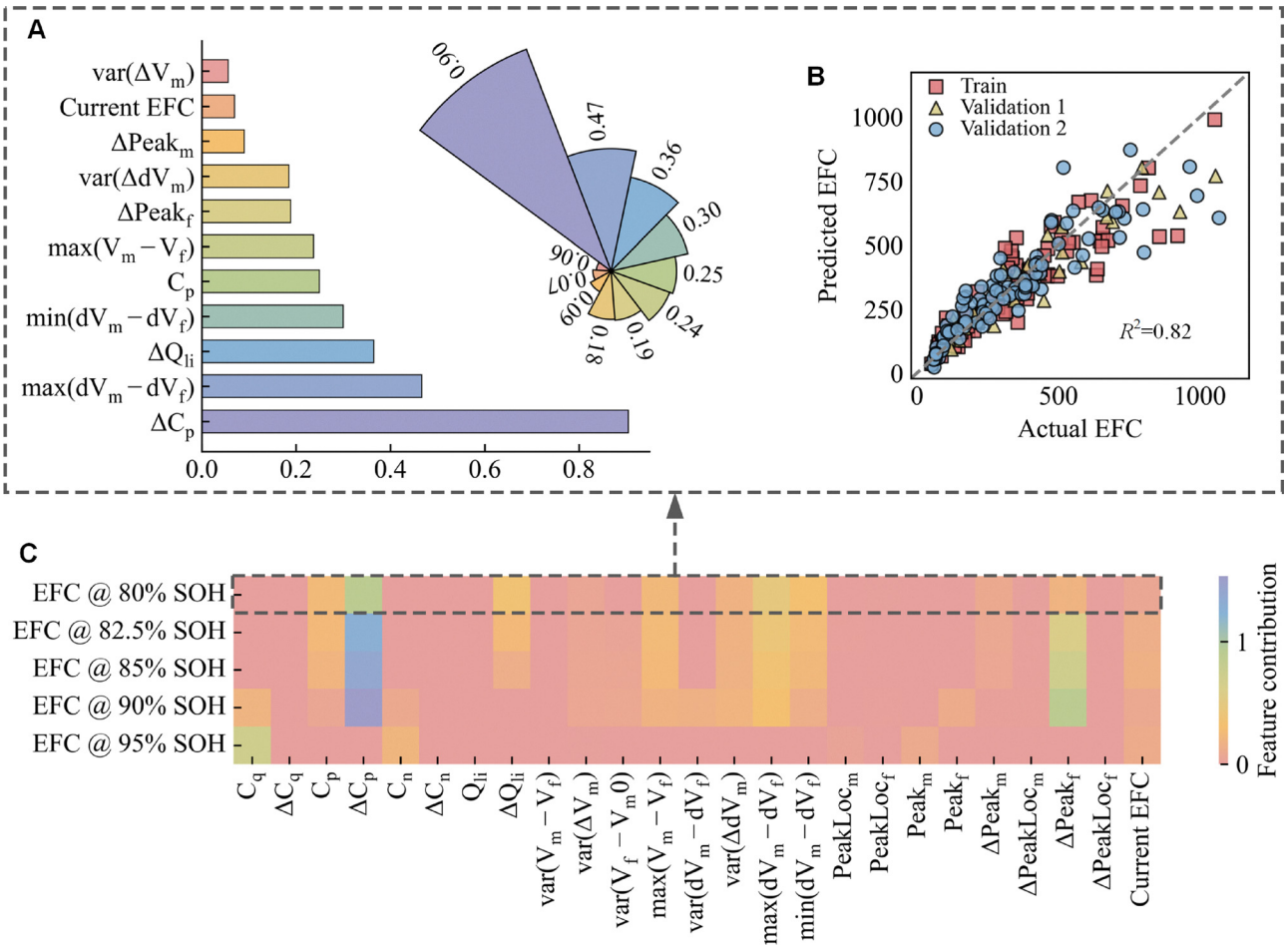

Fig. 6 Cycle life prediction. (A) Feature importance interpretation for the machine learning model in early cycle life until 80% SOH prediction from 30th EFC. (B) Prediction results for the training, validation 1, and validation 2 in early cycle life until 80% SOH from 30th EFC. (C) Feature importance interpretation using the Lasso model for cycle life predictions until SOH drops to different degrees.

Table 2 Summary of the cycle life prediction

SOH threshold	Training/validation	RMSE (EFC)	MAE (EFC)	R^2
95% SOH	Training	6.95	4.18	0.78
	Validation 1	8.89	5.05	0.75
	Validation 2	5.00	3.44	0.88
90% SOH	Training	26.15	17.57	0.86
	Validation 1	30.48	19.60	0.88
	Validation 2	27.29	20.22	0.83
85% SOH	Training	58.45	40.40	0.84
	Validation 1	68.97	48.62	0.86
	Validation 2	56.17	40.76	0.84
82.5% SOH	Training	75.13	50.42	0.83
	Validation 1	78.79	56.67	0.87
	Validation 2	75.93	54.55	0.82
80% SOH	Training	94.45	64.80	0.81
	Validation 1	92.62	64.29	0.87
	Validation 2	101.70	68.50	0.80

generalizability. Additional results using a random split of different cells are in Table S2.

The MAE of early cycle life prediction until 80% SOH remains below 65 and 69 cycles for validation sets 1 and 2, respectively, with corresponding R^2 values exceeding 0.8. The model accurately predicts cells with diverse aging trajectories, with both training and validation data closely aligning with the ideal parity line. However, predictive performance diminishes for cells with longer cycle lives, primarily due to data imbalance, as the model is more influenced by the abundant short-life data. Feature importance analysis of the interpretable model reveals that variations in positive electrode capacity and features derived from differential voltage curves play dominant roles. Notably, features from the negative electrode become increasingly significant when predicting cycle life at higher SOH levels. The peak positions and overall shape of differential voltage curves consistently contribute across different health stages. More prediction results are provided in Fig. S13. Note that the interpretation of the model reflects the feature contribution for the prediction, indicating the numerical data pattern learned from the machine learning model that is not aware of physics. The intrinsic relationship between the feature contribution and the actual dominating aging mechanisms needs further investigation. This is exemplified by predictions from later stages (around 85% SOH), where features linked to the negative electrode become more influential (Fig. S14).

In addition, the model is intrinsically interpretable, eliminating the need for *post hoc* explanation techniques such as SHAP (SHapley Additive exPlanations). To validate the robustness of feature importance, we conducted an additional analysis using XGBoost regression with SHAP-based interpretation. Comparable key features emerge, supporting the consistency of feature contributions across different model architectures (Fig. S15). By employing inherently interpretable models for rate-adaptive prediction, residual compensation, and cycle life forecasting, the underlying predictive mechanisms become more transparent. Overall, features related to electrode health and differential voltage curves play a significant role in early-stage cycle life prediction, and the improved diagnostic insight ensures both the reliability and interpretability of the proposed approach.

3 Conclusion

Understanding battery aging modes typically relies on half-cell analysis to evaluate electrode degradation and loss of active lithium, thereby supporting more comprehensive health diagnostics and improved cycle life prediction. This article first provides a systematic analysis of the key factors affecting DVF, and outlines practical recommendations for achieving reliable fitting, an area that has not been thoroughly investigated before. An interpretable and lightweight C-rate adaptive prediction model is proposed to transform high C-rate mechanistic states into their low C-rate counterparts, enabling faster health assessment without the need for time-consuming low C-rate tests.

To address the challenges of DVF degradation caused by kinetic limitations, material blending, and especially battery aging, we introduce an additional interpretable residual model. This model successfully compensates for fitting errors and reconstructs more realistic degradation trajectories while preserving the critical aging mechanisms. The combination of the C-rate adaptive prediction model and residual compensation model allows a more accurate reconstruction of degradation curves under low C-rate conditions, which are often impractical to measure directly. The combined model achieves a mean absolute voltage error of less than 3.4 mV. Notably, the residual model remains interpretable and robust across batteries subjected to various aging protocols.

Lastly, early-stage cycle life prediction is accomplished using another interpretable model that leverages mechanistic features extracted from both half-cell and differential voltage curves. The model provides accurate and explainable predictions of battery lifespan under different SOH thresholds. When using data from only the first 30 cycles, the model achieves a mean absolute EFC error of less than 70 even under complex and previously unseen aging scenarios. This article concludes with the key insights for battery assessment and proposes interpretable models for systematically enhanced diagnosis and prognosis. Future efforts could focus on further aligning machine learning-based insights with underlying physical aging mechanisms, together with the mechanistic modeling of the DVF residuals.

4 Methods

4.1 Experiment

Battery cycling aging with periodic RPT, including measured OCV curves, is conducted on Datasets 2 and 3.[13,24] Both datasets involve batteries with silicon oxide–graphite blended anodes and nickel–cobalt–aluminum (NCA) cathodes, though the specific types differ. In Dataset 2, cells are aged under constant current cycling with varying C-rates and DODs, while Dataset 3 employs dynamic cycling using diverse real-world protocols. There are 126 cycling conditions consisting of different DOD, charge and discharge protocols sets in Dataset 2, while Dataset 3 considers urban, highway, and real city protocols with C rates ranging from 1/10 to 2C. These experimental conditions yield a wide range of degradation trajectories, capturing the complex aging behaviors observed in practical applications. To evaluate battery health, periodic RPTs are performed, including pseudo-OCV tests at C/5 for Dataset 2 and C/40 for Dataset 3. Following aging to different SOH under various protocols in Dataset 2, a subset of 94 cells is selected for additional testing under both C/5 and C/40 conditions to acquire corresponding pseudo-OCV curves. Additionally, half-cell OCP measurements are conducted on pristine cells at both C/5 and C/40, providing reference data for DVF modeling. The cells are tested through Maccor Series 4000 battery cyclers and kept at an environmental temperature of 25 °C in CSZ ZP-16-2-H/AC chambers for Dataset 2[24] and 25 °C for Dataset 3.[13] More details of the experiment platform and protocols can be found in ref. 13, 24 and 31. To validate the proposed interpretable models, including C-rate-adaptive predictions, residual compensations, and early cycle life predictions, multiple data splitting strategies are used. These include both random splits and scenarios with unseen test sets. Detailed cell assignments for the unseen tests in Dataset 2 are provided in ref. 31.

4.2 Battery health diagnosis model

DVF modeling the relationship between the half-cell OCP curves and full-cell OCV measurement by scaling and shifting the referenced OCP curves. It is a tool for nondestructive battery health diagnosis, and electrode aging conditions are able to be estimated. The expression of the DVF model is[22,24,25,27,34]

$$\mathrm{OCV}(z) = \mathrm{OCP_p}(y) - \mathrm{OCP_n}(x), \tag{1}$$

where $\mathrm{OCP_p}$ and $\mathrm{OCP_n}$ are the half-cell OCPs for the cathode and anode with respect to the lithiation states y and x respectively. The relationship between the full-cell charge state and half-cell lithiation state can be described by

$$z = \frac{Q}{C} = \frac{y - y_{100}}{y_0 - y_{100}} = \frac{x_{100} - x}{x_{100} - x_0}, \tag{2}$$

where Q and C are the available capacity and total capacity, y_{100}, x_{100}, y_0, and x_0 determine the utilization window (100 respect to the final lithiated state while 0 indicates the final delithiated

state) of the half-cell OCPs with respect to the DOD of the full cell. The capacity relationships between the electrodes and the full cell are described by

$$C = C_p(y_0 - y_{100}) = C_n(x_{100} - x_0), \quad (3)$$

where C_p and C_n represent the capacity of the cathode and anode respectively. Then, the normalized lithium concentration at each electrode can be rewritten as

$$y = y_{100} + \frac{Q}{C_p}, \quad x = x_{100} - \frac{Q}{C_n}. \quad (4)$$

Therefore, the full-cell OCV can be described by

$$\mathrm{OCV}(z) = \mathrm{OCP}_p\left(y_{100} + \frac{Q}{C_p}\right) - \mathrm{OCP}_n\left(x_{100} - \frac{Q}{C_n}\right). \quad (5)$$

Therefore, the mechanistic states that determine the full-cell OCV are [C_p, C_n, x_0, y_0]. By applying optimization algorithms such as PSO, DE, BO, GA, and CMA-ES, the four mechanistic states can be effectively estimated through appropriate loss function designs. Detailed descriptions of these optimization methods are provided in Note S1. Several loss functions are constructed to evaluate the fitting performance. First, the mean squared error (MSE) is used to directly compare the measured and fitted voltage curves. Second, the MSE of the differential voltage curves is introduced to highlight the accurate reconstruction of the derivative features. Lastly, a Euclidean distance-based loss is employed to preserve the overall shape of the curves by minimizing the point-wise distance between fitted and measured curves. These loss functions are defined by

$$\mathrm{Loss}_{\mathrm{MSE}} = \frac{1}{N}\sum_{i=1}^{N}\left(\hat{V}_i - V_i\right)^2 \quad (6)$$

$$\mathrm{Loss}_{\mathrm{derivative}} = \frac{1}{N}\sum_{i=1}^{N}\left(\frac{\mathrm{d}\hat{V}}{\mathrm{d}Q}(Q_i) - \frac{\mathrm{d}V}{\mathrm{d}Q}(Q_i)\right)^2 \quad (7)$$

$$\mathrm{Loss}_{\mathrm{euclidean}} = \frac{1}{N}\sum_{i=1}^{N}\min_j \sqrt{(Q_i - Q_j)^2 + (V_i - \hat{V}_j)^2} \quad (8)$$

4.3 Machine learning

Machine learning models are developed to address three key tasks: C-rate adaptive prediction, residual compensation, and early cycle life prediction. For the C-rate adaptive task, mechanistic features extracted from the DVF model at C/5 are used to predict the corresponding states at C/40, effectively mapping high-rate behavior to its low-rate equivalent. In the residual compensation model, both the DVF-fitted curve and the associated mechanistic features serve as inputs to predict the residuals between the reconstructed and actual voltage curves. When the same residual correction is applied to different C-rates, the input features predicted from the C-rate adaptive model are used to ensure consistency. For early cycle life prediction, the model utilizes a combination of mechanistic features derived from the fitted DVF model and differential voltage features, including their evolution relative to the initial cycle, as well as the macroscopic features.[13,24,60–62] These inputs enable accurate predictions of EFCs under various SOH thresholds. A detailed summary of the feature sets used in each model is provided in Note S2.

For the machine learning models, we employ (multi-task) Lasso (Least Absolute Shrinkage and Selection Operator) regression to capture the underlying mappings between features and targets.[63–65] The objective function is formulated as

$$\hat{\mathbf{B}} = \arg\min_{\mathbf{B}}\left\{\frac{1}{2n}\| \mathbf{Y} - \mathbf{XB} \|_F^2 + \lambda\sum_{j=1}^{p}\| \mathbf{B}_j, \|_2\right\} \quad (9)$$

where $\mathbf{X} \in R^{n\times p}$ denotes the input feature matrix with n samples and p features, and $\mathbf{Y} \in R^{n\times T}$ is the response matrix corresponding to T tasks. The model learns a coefficient matrix $\mathbf{B} \in R^{p\times T}$, where each column corresponds to a task-specific regression vector, and each row $\mathbf{B}_j$, contains the coefficients of the jth feature across all tasks. When $T = 1$, the coefficient matrix $\mathbf{B}$ degenerates to a vector $\beta \in R^p$, and the multi-task Lasso objective reduces to the standard Lasso regression formulation with an ℓ_1-norm regularization. The first term in the objective function, $\frac{1}{2n}\|\mathbf{Y} - \mathbf{XB}\|_F^2$, represents the empirical loss aggregated across tasks *via* the Frobenius norm. The second term, $\lambda\sum_{j=1}^{p}\left\|\mathbf{B}_{j,\cdot}\right\|_2$, is a structured regularization penalty that encourages group sparsity across tasks. Specifically, the term applies the ℓ_2 norm across each feature's coefficients (*i.e.*, across tasks), and then sums over all features, which is equivalent to the $\ell_{2,1}$ norm of $\mathbf{B}$. As a result, if a particular feature is not informative for any task, its entire row in $\mathbf{B}$ will be driven to zero. The regularization parameter $\lambda > 0$ controls the trade-off between minimizing prediction error and enforcing sparsity.

Model interpretability arises naturally through the learned coefficient matrix. For each feature j, its overall contribution across tasks is measured by the ℓ_2 norm of the corresponding row, *i.e.*, $||\mathbf{B}_j,||_2$. A larger norm indicates that the feature has a stronger influence on at least one task. This allows for intuitive ranking of feature contributions and identification of shared predictors across multiple outputs, making the model inherently interpretable in multi-task settings.

Author contributions

Conceptualization, Y. C., W. C. C., and R. D. B.; methodology, Y. C., J. S., J. R., L. W., P. A. A., W. C. C., and R. D. B.; investigation, Y. C., J. S., and P. A. A.; writing – original draft, Y. C., J. S., J. R., and R. D. B.; writing – review & editing, L. W., M. K., J. S., R. F., M. Z. B., W. C. C., and R. D. B.; funding acquisition, M. Z. B., W. C. C., R. D. B., and Y. C.; resources, M. Z. B., W. C. C., and R. D. B.; supervision, M. Z. B., W. C. C., and R. D. B.

Conflicts of interest

The authors declare no conflicts of interest.

Data availability

The data used in this paper are available through https://data.matr.io/10/ for Dataset 1,[31] https://data.matr.io/11/ for Dataset 2,[24] and https://purl.stanford.edu/td676xr4322 for Dataset 3.[13] The code is available as supplementary information (SI). Supplementary information is available. See DOI: https://doi.org/10.1039/d5ee06439b.

Acknowledgements

This work was supported by the Toyota Research Institute through the D3BATT program. Y. C. acknowledges the Novo Nordisk Foundation.

References

1 V. Viswanathan, A. H. Epstein, Y.-M. Chiang, E. Takeuchi, M. Bradley, J. Langford and M. Winter, *Nature*, 2022, **601**, 519–525.
2 Y. Shi and J. H. Pikul, *Sci. Rob.*, 2025, **10**, eadr6125.
3 L. Li, J. Yang, R. Tan, W. Shu, C. J. Low, Z. Zhang, Y. Zhao, C. Li, Y. Zhang and X. Li, *et al.*, *Nat. Chem. Eng.*, 2024, **1**, 542–551.
4 Y. Che, X. Hu, X. Lin, J. Guo and R. Teodorescu, *Energy Environ. Sci.*, 2023, **16**, 338–371.
5 A. Thelen, X. Huan, N. Paulson, S. Onori, Z. Hu and C. Hu, *npj Mater. Sustain.*, 2024, **2**, 14.
6 M. Dubarry, N. Costa and D. Matthews, *Nat. Commun.*, 2023, **14**, 3138.
7 S. Tao, M. Zhang, Z. Zhao, H. Li, R. Ma, Y. Che, X. Sun, L. Su, C. Sun and X. Chen, *et al.*, *Energy Environ. Sci.*, 2025, **18**, 1544–1559.
8 N. Qin, L. Jin, Y. Lu, Q. Wu, J. Zheng, C. Zhang, Z. Chen and J. P. Zheng, *Adv. Energy Mater.*, 2022, **12**, 2103402.
9 M. Broussely, P. Biensan, F. Bonhomme, P. Blanchard, S. Herreyre, K. Nechev and R. J. Staniewicz, *J. Power Sources*, 2005, **146**, 90–96.
10 M. Börner, A. Friesen, M. Grützke, Y. P. Stenzel, G. Brunklaus, J. Haetge, S. Nowak, F. M. Schappacher and M. Winter, *J. Power Sources*, 2017, **342**, 382–392.
11 R. Xiong, Y. Pan, W. Shen, H. Li and F. Sun, *Renewable Sustainable Energy Rev.*, 2020, **131**, 110048.
12 I. Kim, H. Kim, S. An, J. Oh, M. Kim and J. W. Choi, *Energy Environ. Sci.*, 2025, **18**, 3784–3794.
13 A. Geslin, L. Xu, D. Ganapathi, K. Moy, W. C. Chueh and S. Onori, *Nat. Energy*, 2025, **10**, 172–180.
14 B.-R. Chen, C. M. Walker, S. Kim, M. R. Kunz, T. R. Tanim and E. J. Dufek, *Joule*, 2022, **6**, 2776–2793.
15 W. Guo, Z. Sun, J. Guo, Y. Li, S. B. Vilsen and D. I. Stroe, *Adv. Energy Mater.*, 2024, **14**, 2401644.
16 R. Li, N. D. Kirkaldy, F. F. Oehler, M. Marinescu, G. J. Offer and S. E. O'Kane, *Nat. Commun.*, 2025, **16**, 2776.
17 S. Dey, Y. Shi, K. Smith, A. M. Colclasure and X. Li, *IEEE Trans. Ind. Electron.*, 2019, **67**, 2167–2175.
18 S. Atalay, M. Sheikh, A. Mariani, Y. Merla, E. Bower and W. D. Widanage, *J. Power Sources*, 2020, **478**, 229026.
19 S. Kim, Z. Yi, B.-R. Chen, T. R. Tanim and E. J. Dufek, *Energy Storage Mater.*, 2022, **45**, 1002–1011.
20 J. Chen, X. Han, T. Sun and Y. Zheng, *Appl. Energy*, 2024, **356**, 122330.
21 H. Kim, I. Kim, M. Kim, S. An, H. C. Ahn, D. Park, J. H. Lee, C. Y. Kang and J. W. Choi, *Proc. Natl. Acad. Sci. U. S. A.*, 2025, **122**, e2424838122.
22 S. Lee, J. B. Siegel, A. G. Stefanopoulou, J.-W. Lee and T.-K. Lee, *J. Electrochem. Soc.*, 2020, **167**, 090531.
23 C. R. Birkl, E. McTurk, M. Roberts, P. Bruce and D. Howey, *J. Electrochem. Soc.*, 2015, **162**, A2271.
24 B. van Vlijmen, V. N. Lam, P. A. Asinger, X. Cui, J. Schaeffer, A. Geslin, D. Ganapathi, S. Sun, P. K. Herring and C. B. Gopal, *et al.*, *Energy Environ. Sci.*, 2025, **18**, 6641–6654.
25 A. Marongiu, N. Nlandi, Y. Rong and D. U. Sauer, *J. Power Sources*, 2016, **324**, 158–169.
26 D. Lu, M. S. Trimboli, G. Fan, R. Zhang and G. L. Plett, *J. Electrochem. Soc.*, 2021, **168**, 070533.
27 M. Dubarry, C. Truchot and B. Y. Liaw, *J. Power Sources*, 2012, **219**, 204–216.
28 T. Hofmann, J. Hamar, B. Mager, S. Erhard and J. P. Schmidt, *Energy AI*, 2024, **17**, 100382.
29 Z. Zhou, Y. Liu, C. Zhang, W. Shen and R. Xiong, *J. Energy Chem.*, 2024, **90**, 120–132.
30 C.-J. Ko and K.-C. Chen, *Appl. Energy*, 2024, **357**, 122488.
31 Y. Che, V. N. Lam, J. Rhyu, J. Schaeffer, M. Kim, M. Z. Bazant, W. C. Chueh and R. D. Braatz, *Joule*, 2025, **9**, 102010.
32 F. Wang, Z. Zhai, Z. Zhao, Y. Di and X. Chen, *Nat. Commun.*, 2024, **15**, 4332.
33 J. Schmitt, M. Schindler and A. Jossen, *J. Power Sources*, 2021, **506**, 230240.
34 J. Schmitt, M. Schindler, A. Oberbauer and A. Jossen, *J. Power Sources*, 2022, **532**, 231296.
35 L. Lavigne, J. Sabatier, J. M. Francisco, F. Guillemard and A. Noury, *J. Power Sources*, 2016, **324**, 694–703.
36 R. Brunetaud, K. M. Mbeya, N. Legrand, O. Briat, A. Capitaine and J.-M. Vinassa, *J. Energy Storage*, 2023, **62**, 106863.
37 T. Hofmann, J. Li, J. Hamar, S. Erhard and J. P. Schmidt, *J. Power Sources*, 2024, **596**, 234107.
38 J. Rhyu, J. Schaeffer, M. L. Li, X. Cui, W. C. Chueh, M. Z. Bazant and R. D. Braatz, *Joule*, 2025, **9**.
39 Y. Zhang, Q. Tang, Y. Zhang, J. Wang, U. Stimming and A. A. Lee, *Nat. Commun.*, 2020, **11**, 1706.
40 S. Tao, C. Sun, S. Fu, Y. Wang, R. Ma, Z. Han, Y. Sun, Y. Li, G. Wei and X. Zhang, *et al.*, *ACS Energy Lett.*, 2023, **8**, 3269–3279.
41 T. Li, Z. Zhou, A. Thelen, D. A. Howey and C. Hu, *Cell Rep. Phys. Sci.*, 2024, **5**.
42 L. Sugiarto, Z. Huang and Y.-C. Lu, *Energy Environ. Sci.*, 2025, **18**, 2511–2523.
43 K. A. Severson, P. M. Attia, N. Jin, N. Perkins, B. Jiang, Z. Yang, M. H. Chen, M. Aykol, P. K. Herring, D. Fraggedakis,

M. Z. Bazant, S. J. Harris, W. C. Chueh and R. D. Braatz, *Nat. Energy*, 2019, **4**, 383–391.
44 N. H. Paulson, J. Kubal, L. Ward, S. Saxena, W. Lu and S. J. Babinec, *J. Power Sources*, 2022, **527**, 231127.
45 N. Guo, S. Chen, J. Tao, Y. Liu, J. Wan and X. Li, *Joule*, 2024, **8**, 1820–1836.
46 H. Zhang, Y. Li, S. Zheng, Z. Lu, X. Gui, W. Xu and J. Bian, *Nat. Mach. Intell.*, 2025, **7**, 270–277.
47 Y. Yang, *Appl. Energy*, 2021, **292**, 116897.
48 J. Schaeffer, E. Lenz, W. C. Chueh, M. Z. Bazant, R. Findeisen and R. D. Braatz, *Comput. Chem. Eng.*, 2024, **180**, 108471.
49 P. Gasper, N. Prakash, J. Schaeffer, R. Findeisen and K. L. Harrison, *J. Electrochem. Soc.*, 2025, **172**, 043509.
50 J. Lin and E. Khoo, *J. Power Sources*, 2024, **605**, 234446.
51 Q. Liang and M. Z. Bazant, *J. Electrochem. Soc.*, 2023, **170**, 093510.
52 W. Dreyer, J. Jamnik, C. Guhlke, R. Huth, J. Moškon and M. Gaberšček, *Nat. Mater.*, 2010, **9**, 448–453.
53 T. R. Ferguson and M. Z. Bazant, *Electrochim. Acta*, 2014, **146**, 89–97.
54 Y. Li, F. El Gabaly, T. R. Ferguson, R. B. Smith, N. C. Bartelt, J. D. Sugar, K. R. Fenton, D. A. Cogswell, A. D. Kilcoyne and T. Tyliszczak, *et al.*, *Nat. Mater.*, 2014, **13**, 1149–1156.
55 M. Z. Bazant, *Faraday Discuss.*, 2017, **199**, 423–463.
56 P. M. Attia, A. A. Bills, F. B. Planella, P. Dechent, G. D. Reis, M. Dubarry, P. Gasper, R. Gilchrist, S. Greenbank, D. Howey, O. Liu, E. Khoo, Y. Preger, A. Soni, S. Sripad, A. Stefanopoulou and V. Sulzer, *J. Electrochem. Soc.*, 2022, **169**.
57 D. Fraggedakis, N. Nadkarni, T. Gao, T. Zhou, Y. Zhang, Y. Han, R. M. Stephens, Y. Shao-Horn and M. Z. Bazant, *Energy Environ. Sci.*, 2020, **13**, 2142–2152.
58 R. B. Smith and M. Z. Bazant, *J. Electrochem. Soc.*, 2017, **164**, E3291.
59 H. Lian and M. Z. Bazant, *J. Electrochem. Soc.*, 2024, **171**, 010526.
60 C. She, Z. Wang, F. Sun, P. Liu and L. Zhang, *IEEE Trans. Ind. Inf.*, 2019, **16**, 3345–3354.
61 Q. Wang, Z. Wang, P. Liu, L. Zhang, D. U. Sauer and W. Li, *Cell Rep. Phys. Sci.*, 2023, **4**.
62 D. Lyu, B. Zhang, E. Zio and J. Xiang, *Cell Rep. Phys. Sci.*, 2024, **5**.
63 R. Tibshirani, *J. R. Stat. Soc. Ser. B: Stat. Methodol.*, 1996, **58**, 267–288.
64 L. Meier, S. Van De Geer and P. Bühlmann, *J. R. Stat. Soc. Ser. B: Stat. Methodol.*, 2008, **70**, 53–71.
65 S. Lee, J. Zhu and E. Xing, *Advances in Neural Information Processing Systems*, 2010.

